GSICS Global Space-based Inter-Calibration System

Quarterly

doi: 10.25923/6c4m-y998

Newsletter Winter 2024 Issue

Editor: Manik Bali (ESSIC/UMD)

CMA • CNES • ESA • EUMETSAT • IMD • ISRO • JAXA • JMA • KMA • NASA • NIST • NOAA • ROSCOSMOS . ROSHYDROMET • SITP • USGS • WMO

Articles

News in This Quarter

Announcements

GSICS Related Publications

Mid-Tropospheric Layer Temperature Record Derived from Satellite Microwave Sounder Observations with Backward Merging Approach

By C.-Z. Zou (NOAA), H. Xu (UMD), X. Hao (GMU), and Q. Liu (GMU)

We present here a new version (V5.0) of the NOAA Center for Satellite Applications and Research (STAR) mid-tropospheric layer temperature (TMT, roughly peaking at 5 km), climate data record (CDR). This TMT CDR is a global dataset with 2.5°x2.5° latitude/longitude grid resolution covering the period from late 1978 to present. In this CDR, we merge microwave sounder observations from 16 polar-orbiting satellites including the NOAA Polar-orbiting Operational Environmental Satellite (POES) series (TIROS-N to NOAA-19), MetOp-A, NASA Aqua, and NOAA Joint Polar Satellite System (JPSS) series (SNPP and NOAA-20).

These platforms host multiple Microwave sensors that include Microwave Sounding Unit (MSU) during 1979-2004, Advanced Microwave Sounding Unit-A (AMSU-A) during 1998-2017, and Advanced Technology Microwave Sounder (ATMS) from 2012 to present.

A backward merging approach was used to intercalibrate multiple satellite data records, in which earlier satellites were adjusted and merged to a reference time series constructed from recent satellite observations in stable orbits after 2002 (Aqua, MetOp-A, SNPP, and NOAA-20). The reference time series has a high accuracy in climate trend detection, allowing intercalibration and trend detection with better accuracy in time series of the entire period from late 1978 to present.

A comprehensive investigation on bias correction algorithms for different error sources, including those from different incident angels, diurnal sampling errors, calibration drift, channel frequency differences between MSU and AMSU-A channels, and solar-heating induced warm target effect on observed brightness temperature was conducted. Investigation revealed that the calibration drift and diurnal sampling drift significantly affect the long-term trends in the merged TMT time series. This review only focuses on removal of bias drifts from these two sources.

Zou et. al., 2011 & 2023 describe the recalibration algorithm for removing calibration drift. The algorithm exploits simultaneous nadir overpass (SNO) matchups to derive inter-calibration coefficients in the level-1 instrument calibration equation. AMSU/MSU sounders usually use cold space views and internal blackbody warm target views to calibrate scene temperatures from the Earth views. In pre-launch operational calibration, calibration coefficients in the calibration equation were obtained from thermal-vacuum chamber test data. In the post-launch recalibration, calibration coefficients were assumed to vary linearly over time and these time-varying coefficients were obtained from SNO

doi: 10.25923/6c4m-y998

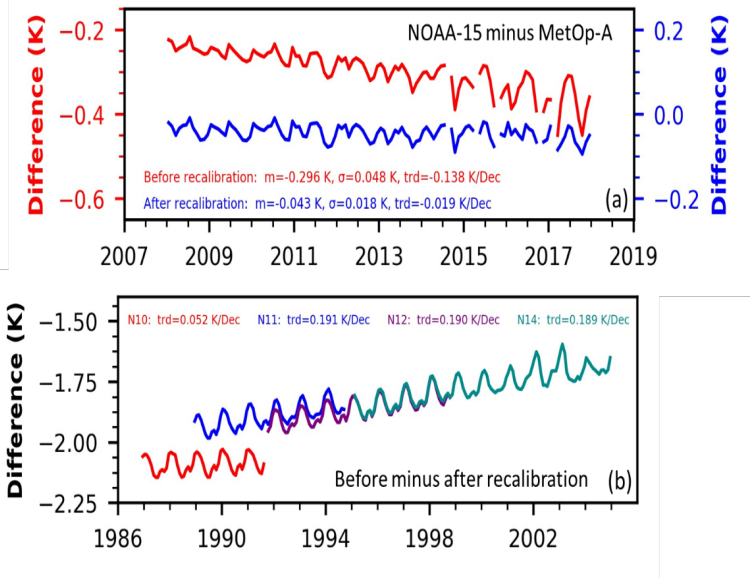

Figure 1. a) Inter-satellite difference time series of global ocean mean brightness temperatures of AMSU-A channel 5 between NOAA-15 and MetOp-A, for before and after recalibration. b) Global mean difference time series for before minus after recalibration for MSU channel 2 observations onboard NOAA-10 through NOAA-14. Plots are from Zou et al. (2023).

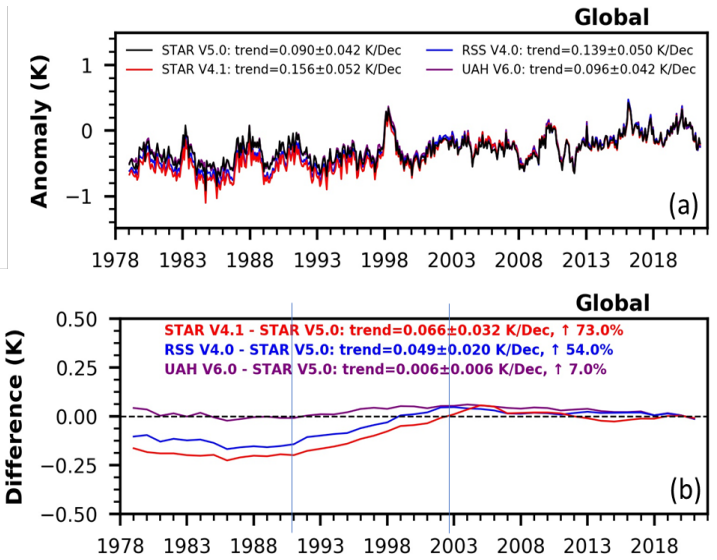

Figure 2. Comparisons of TMT time series between existing datasets and STAR V5.0 during January 1979–June 2021. a) Deseasonalized global-mean TMT monthly anomalies; (b) Global annual mean anomaly differences between existing datasets and STAR V5.0.

regressions. However, the regression coefficients still display calibration drifts. These calibration drifts can be explained by three possible mechanisms:

i) time-varying side-lobe effect resulting from possible degradation in reflector or antenna materials

ii) possible change over time in the blackbody warm target emissivity (The blackbody temperature is measured by the platinum resistance thermometers (PRTs) embedded in the blackbody target, but a degradation in blackbody emissivity could cause a bias drift in the blackbody radiometric temperature.)

iii) degradation in detector or amplifier may cause changes in calibration nonlinearity, which causes calibration bias drift as well as solar heating related seasonal variability in brightness temperature.

In Figure 1a, the NOAA-15 AMSU-A channel 5 observations showed a cooling drift relative to the same channel observations onboard MetOp-A during 2007-2017 and a solar-heating induced brightness temperature variability after 2015. Zou et al. 2023 recalibration successfully removed the cooling drift and reduced the variability. In addition, recalibration also removed spurious warming drifts in the MSU channel 2 observations onboard NOAA-11 through NOAA-14 (Figure 1b). This made the observations from NOAA-11 through NOAA-14 consistent with the reference observations from satellites in stable orbits. However, this does not address diurnal variations in biases.

To address diurnal biases, the correction algorithms are complemented by an innovative semi-physical diurnal model which attempts to simulate diurnal biases through physical and empirical equations. Diurnal drifting errors are typically caused by orbital drifts with satellites from TIROS-N through NOAA-19. The diurnal model assumes that diurnal temperature changes are cosine functions of the satellite local equator crossing time (LECT), with both diurnal and semi-diurnal components being included in the cosine functions. The actual diurnal air temperature changes follow a quasi-sinusoidal pattern during daytime and a thermal decay process during nighttime. The model is physically based during daytime and an empirical model during nighttime. The amplitudes and phases of the cosine functions are resolved using regressions of satellite overlapping observations. The model simulates the satellite ascending and descending diurnal cycles separately to account for different physical processes during daytime and nighttime. These processes enable the diurnal model to mitigate the diurnal drifting errors and result in inter-consistent observations between the reference and earlier satellites with orbital drifts.

To validate the new CDR (STAR V5.0 TMT) it was compared with existing

datasets developed by other research groups, including the University of Alabama at Huntsville (UAH V6.0, Spencer et al. 2017), Remote Sensing Systems (RSS V4.0, Mears et al. 2016), and an early version of the STAR TMT (STAR V4.1, Zou and Wang 2011). Different versions of the anomaly time series show excellent agreement in variability (Figures 2a). Diurnal sampling drift generally has large impact on the TMT trend. However, since all the existing versions of TMT have already included diurnal drift adjustments, although with different adjusting algorithms, impact from the diurnal drift adjustment on their trend differences relative to STAR V5.0 are not obvious. Instead, removal of the spurious warming drifts in NOAA-11 through NOAA-14 in STAR V5.0 significantly lowered its warming trend relative to STAR V4.1 and RSS V4.0 during 1991-2002 and the entire observation period from late 1978 to present (Figure 2b). In this Figure time series are plotted so that their mean differences during 01/2020–06/2021 are zero. Vertical lines in Figure 2 b) represent the end of NOAA-10 near 1991 and start of Aqua on August 2002, respectively.

During 1991-2002, the STAR V.4.1 and RSS 4.0 exhibited a similar large upward trend relative to STAR V5.0. This occurred because recalibration in STAR V5.0 had removed the suprious warming drifts in NOAA-11 through NOAA-14. Plots are from Zou et al. (2023).

The smaller warming trends in STAR V5.0 TMT have strong implications for trends in climate model simulations. Based on TMT and the lower-stratospheric temperature time series, the paper derived a Total Tropospheric Temperature (TTT) representing tropospheric layers from the Earth's surface to about 10 km above. Compared with model simulations from the Coupled Model Inter-Comparison Project, Phases 5 and 6 (CMIP5 and CMIP6), the STAR V5.0 TTT trend was only one-half of the climate model simulations during 1979-present. This may suggest deficiencies in climate model simulations that need to be improved in order to accurately represent the climate reality.

Disclaimer: The views and opinions contained in this report are those of the authors and should not be construed as an official NOAA or U.S. Government position, policy, or decision.

References

Mears, C. A., and F. J. Wentz, 2016: Sensitivity of satellite-derived tropospheric temperature trends to the diurnal cycle adjustment. *J. Clim*. **29**, 3629–3646.

Spencer, R.W., J. R. Christy, W. D. Braswell, 2017: UAH version 6 global satellite temperature products: Methodology and results, *Asia-Pac. J. Atmos. Sci*. **53**, 121-130.

Zou, C.-Z., and W. Wang, 2011: Inter-satellite calibration of AMSU-A observations for weather and climate applications. *J. Geophys. Res.* **116**, D23113,DOI:10.1029/2011JD016205.

Zou, C.-Z., Xu, H., Hao, X., & Liu, Q. (2023). Mid-tropospheric layer temperature record derived from satellite microwave sounder observations with backward merging approach. J. Geophys. Res.: Atmospheres, **128**, e2022JD037472. https://doi.org/10.1029/20221D037

Effect of Scattering Angle on DSCOVR/EPIC Observations

By Guoyong Wen (NASA/GESTAR) and Alexander Marshak (NASA)

Summary

We have analysed EPIC observed global average reflectance in 2021, the year when the scattering angle reaches the extreme value of 178°. There are four spikes in spectral reflectance in 2021. Those spikes were not detected in 2016 EPIC observations nor in the CERES SW flux. Rather, they coincide with the peaks of scattering angle near 178°. The reflectance enhancement depends strongly on wavelength and is influenced by the change in global average cloud amount. The enhancement is mainly due to low level clouds. We also found that the strong wavelength dependence of the enhancement is primarily due to wavelength dependence of cloud scattering phase function. Radiative transfer calculations show that the change in scattering angles has the largest impact on TOA reflectance in the red and NIR channels at 680 nm and 780 nm and the smallest influence on reflectance in the UV channel at 388 nm, a similar feature in the EPIC observed global reflectance enhancement. The change in cloud amount in a cycle of scattering angle variation also plays an important role in increasing or decreasing the enhancement depending on whether the change in cloud fraction is in phase or out of phase with scattering angle variation.

doi: 10.25923/6c4m-y998

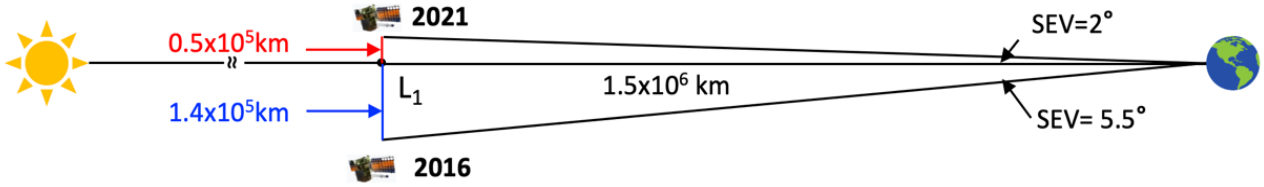

Figure 1. Sketch of Sun, Earth, and DSCOVR satellite vehicle position when the SEV reaches minimum for 2016 and 2021.

Impact of scattering angle on EPIC global average spectral reflectance

The launch of the Deep Space Climate Observatory (DSCOVR) in February 2015 to the orbit around Sun-Earth Lagrange-1 (L_1) point, about 1.5 million kilometers from the Earth, started a new perspective of Earth observations from space. Earth Polychromatic Imaging Camera (EPIC) is an Earth-looking instrument onboard DSCOVR to monitor the Earth. It consists of a 30-cm aperture Cassegrain telescope with a 0.62° field of view encompassing the Earth that has a nominal size of 0.5° at the L_1 point. EPIC provides 10 narrowband spectral images of the entire sunlit side of Earth using a 2048 x 2048 pixel charge-coupled device detector every 65 min (Northern Hemisphere summer) to 111 min (in Northern Hemisphere winter). The wavelength ranges from ultraviolet, visible, to near infrared (NIR). The sampling size on the Earth is nominally 8 x 8 km^2 at the center of the image with an effective spatial resolution of 12 x 12 km^2 for the 443 nm channel when EPIC's point spread function is considered. To reduce the downlink transmission time, the images for all wavelengths, except 443 nm, have been reduced to 1,024 x 1,024 pixels (Herman et al., 2018, Marshak et al., 2018).

The instrument had routinely operated until June 27, 2019, when the spacecraft was placed in an extended safe hold due to degradation of an inertial navigation unit. DSCOVR returned to full operations on March 2, 2020. Since then, the range of the scattering angle between the incident sunlight and sensor direction is larger than it was before and the largest scattering reaches ~178°, only 2° from the perfect back scattering direction. Figure 1 shows a sketch of the Sun, Earth, and Vehicle (satellite) position when the scattering angle reached its upper bound, or the Sun-Earth-Vehicle (SEV) angle reached its lower bound for 2016 and 2021. The minimum SEV angle is ~5.5° and ~2° for 2016 and 2021, respectively. In 2021, the closest distance of the DSCOVR satellite to the Sun-Earth line is ~0.5x10^5 km, only ~2/5 of the closest distance of ~1.4x10^5 for 2016.

Figure 1. Sketch of Sun, Earth, and DSCOVR satellite vehicle position when the SEV reaches minimum for 2016 and 2021.

Studying the impact of near-backward scattering on EPIC top-of-atmosphere (TOA) reflectance, Marshak et al. (2021) and Penttila et al. (2021) show a strong increase in the TOA reflectance towards the backscattering direction. They found that the reflectance increase occurred for both cloudy and clear sky over ocean and land areas (except cloudless areas over ocean); the largest enhancements arise in the NIR from vegetation.

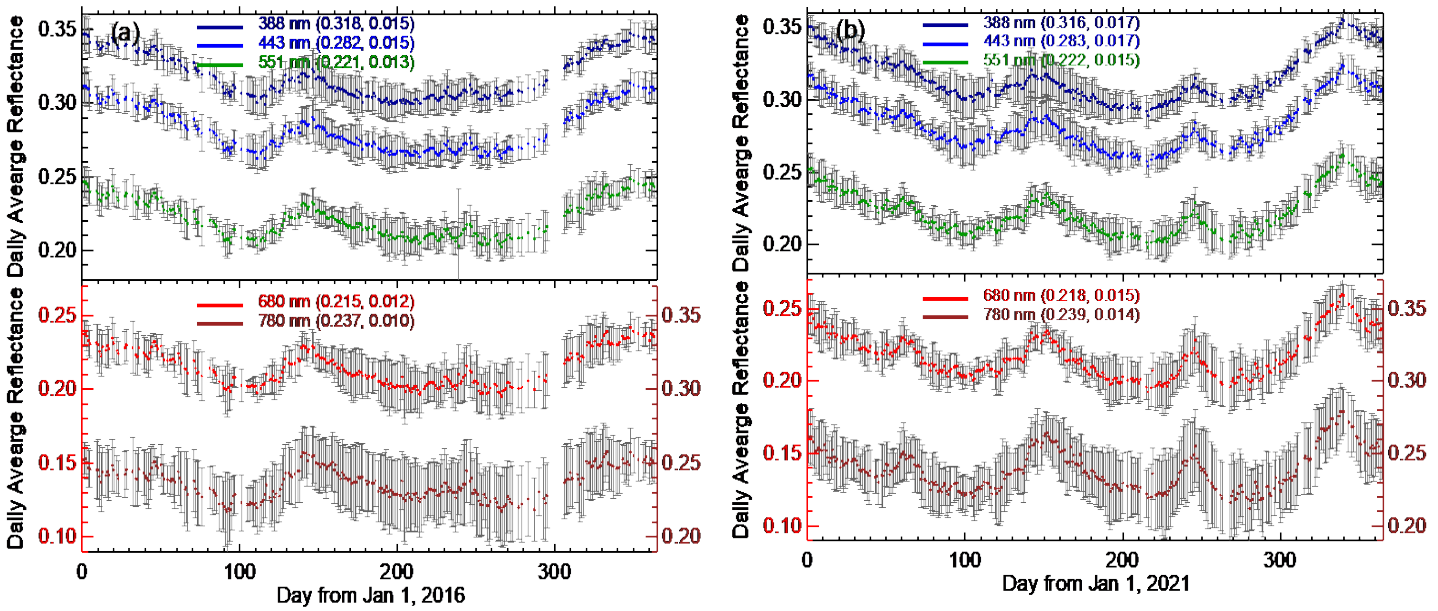

Figure 2. (a) Time series of daily average global reflectance with gray bars for the standard deviations for 2016 and (b) for 2021. The annual mean and standard deviation of daily reflectance are indicated in parenthesis of the legends. Note that the ranges of all vertical axes are the same. The spikes in global spectral reflectance coincide with the peaks of the scattering angle.

doi: 10.25923/6c4m-y998

By comparing daily global average reflectance in five EPIC non-absorbing channels in year 2021 and 2016, it was found that the spectral reflectances in 2021 differ dramatically from 2016 (Fig. 2). There are five distinctive spikes in spectral reflectance in 2021, and magnitude of those spike is wavelength dependent. Those enhanced spectral reflectances are not found in 2016 EPIC data nor in CERES observations. This study focuses on understanding the physical mechanism for the enhanced spectral reflectance based on EPIC observations and radiative transfer calculations.

Mie scattering calculations show that for water clouds with typical effective radius of 10 μm, the phase function increases with scattering angle up to ~178° for all five wavelengths. For a given scattering angle between 170° and 178°, the phase function monotonically increases with wavelength. In fact, the phase function for 780 nm reaches a local maximum at ~178° as the scattering angle increases. At 178°, the maximum EPIC scattering angle, the phase function increases from 0.27 for 388 nm to 0.46 for 780 nm, about a 70% increase. This wavelength dependence of phase function near perfect backscattering angle is the unique feature of the optical phenomenon of glory. This feature is consistent with the wavelength dependence of the EPIC observed enhancement. Full radiative transfer model simulations quantitatively explain the EPIC observed global spectral reflectance enhancement as the scattering approaches near perfect backscattering angle.

Cloud is a unique component of Earth's atmosphere and plays an important role in Earth's radiation budget by reflecting large portion of incident solar radiation. As clouds are so effective reflecting sunlight, the global spectral reflectance in the five non-absorbing absorbing channels is highly correlated with global average cloud fraction as well. Therefore, the change of cloud fraction has a strong impact on EPIC observed global reflectance. Thus, the EPIC observed global reflectance enhancement is a result of the two competing factors – changes of scattering angle and cloud fraction. Thus, the magnitude of reflectance enhancement in a cycle of scattering angle variation depends on whether the change in cloud fraction is in phase or out of phase with scattering angle variation.

References

Herman, J.R., L. Huang, R.D. McPeters, J. Ziemke, A. Cede, and K. Blank (2018). Synoptic ozone, cloud reflectivity, and erythemal irradiance from sunrise to sunset for the whole Earth as viewed by DSCOVR spacecraft from the earth-sun Lagrange-1, *Atmos. Meas. Tech*., 11, 177-194, https://www.atmos-meas-tech.net/11/177/2018/amt-11-177-2018.pdf

Marshak, A., et al. (2018). Earth Observations from DSCOVR/EPIC Instrument. *Bulletin Amer. Meteor. Soc. (BAMS)*, 9, 1829-1850, https://doi.org/10.1175/BAMS-D-17-0223.1.

Marshak, A., Alfonso, Delgado-Bonal, Knyazikhin (2021). Effect of Scattering Angle on Eerth Reflectance, Front. Remote Sens., 2., 2, Effect of Scattering Angle on Earth Reflectance." *Frontiers in Remote Sensing*, **2:** [10.3389/frsen.2021.719610.

Penttilä A., et al. (2022). Temporal variation of the shortwave albedo of the Earth. *Frontiers in Remote Sens.,* 3, doi: 10.3389/frsen.2022.790723

.

A new radiance model for the Moon and other airless planetary bodies

By Kay Wohlfarth and Christian Wöhler (TU Dortmund University, Germany)

We developed a new model that simulates the radiance of the Moon and other airless planetary bodies in the near- and mid-infrared. The model was primarily built to address scientific questions about lunar volatiles and Mercury's mineralogy, but given the high accuracy, it can aid the accurate calibration of Earth-observation satellites. This article summarizes the model from the full paper [1].

Why lunar thermal emission is anisotropic: The lunar surface is sheeted with a particulate material (regolith) layer, forming a rugged and rough surface structure. Roughness occurs down to very small scales of several millimeters and below. Each point of a rough surface is differently oriented toward the sun and thus receives a different amount of solar flux, which causes different temperatures. If the material were conductive, the heat would quickly diffuse and establish a single bulk temperature. However, planetary regolith is highly isolating. It can sustain strong thermal gradients at small scales so that the surface temperature can change by tens to hundreds of degrees within several millimeters. Consequently, a rough planetary surface does not have a single

doi: 10.25923/6c4m-y998

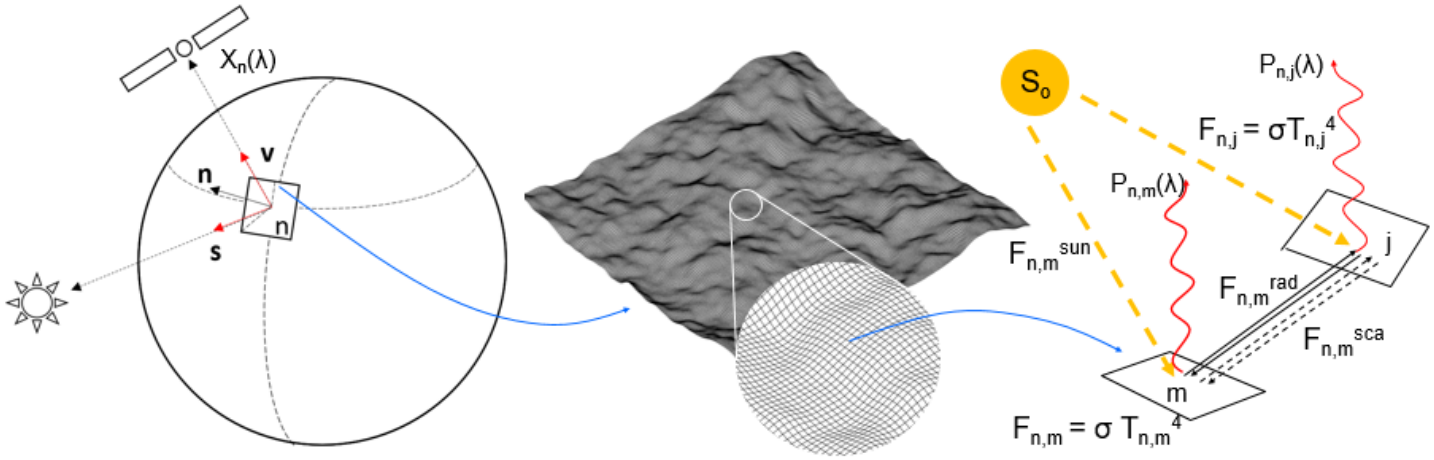

Figure 1: Left: The entire Moon is divided into N facets with an individual illumination configuration. We are interested in the radiance $X_n(\lambda)$ that emerges from the n^{th} facet. Middle: Each facet n is associated with an entire fractal surface [2] that consists of M=40,000 elements (each 1 mm²) and is not resolved by the sensor. Right: Each surface element m from illumination configuration n has a temperature T_{nm} and emits radiation P_{nm}. The sum of the thermal emission P of all fractal surface elements M determines $X_n(\lambda)$. The radiation balance equation gives the temperature of each element m. For more details, see [1].

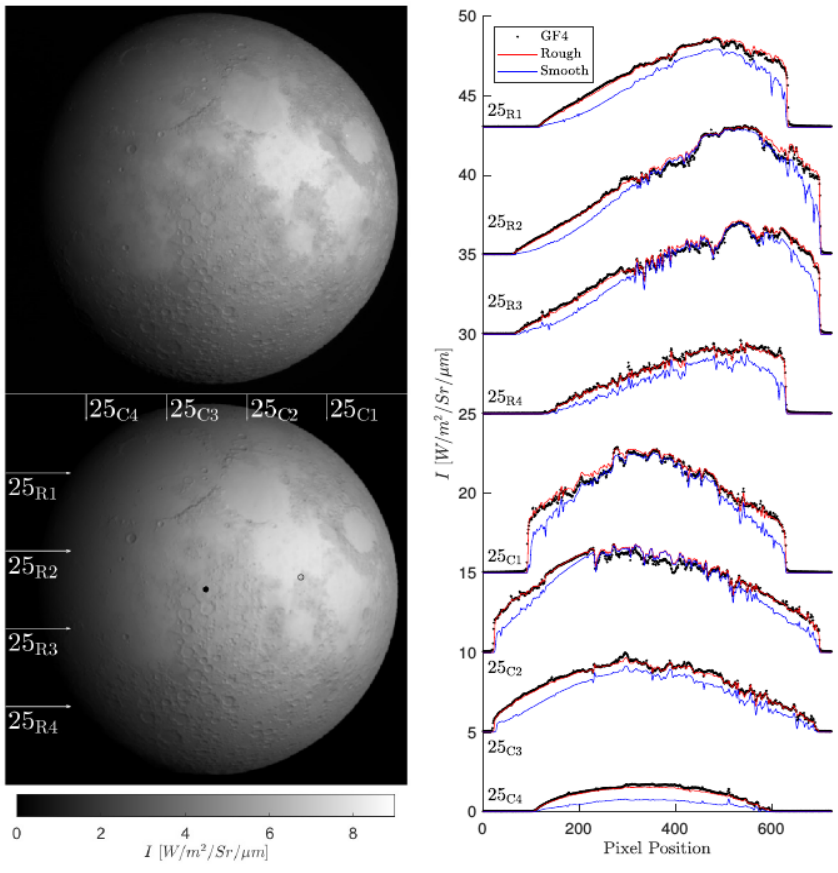

bulk temperature but hosts a distribution of vastly different temperatures. The thermal emission of the surface is then the superposition of many Planck functions with individual temperatures. Because the Planck function is not linear, the thermal emission can no longer be approximated with a Planck. In nadir view and nadir illumination, the thermal emission of the rough surface is the same as for a smooth surface. Suppose the solar illumination direction and the viewing direction roughly fall together. In that case, the detector preferentially sees hotter surface elements; thus, the surface appears to emit more thermal radiation than a smooth surface. If the illumination and the viewing direction point opposite directions, the observer sees more shadows, and the measured thermal emission declines.

Model description: The new thermal model uses fractal rough surfaces constrained with realistic lunar regolith

Figure 2 (Above): Comparison of the Gaofen-4 lunar data with our modeling results. Top Left: Radiance I of the lunar disk at 3.77 µm measured on July 25, 2018, with the GF-4 satellite. Bottom Left: Radiance of the lunar disk simulated with the new model. The arrows indicate the horizontal sampling profiles $25_{\_R1}$ to $25_{\_R4}$ and the vertical sampling profiles $25_{\_C1}$ to $25_{\_C4}$. The gray circle indicates the subsolar point and the black dot stands for the subcamera point. Right: Comparison of the measured radiance (black) with the rough model (red) and the equilibrium model (blue) along the horizontal profiles $25_{\_R1}$ to $25_{\_R4}$ and along the vertical profiles $25_{\_C1}$ to $25_{\_C4}$ indicated on the bottom left. Offsets for clarity. Figure taken from [1].

statistics derived from lunar close-up images [2]. For each fractal surface element, the temperature is computed via a radiation balance equation extending, e.g., upon [3]. For illustration, see Figure 1. An efficient numerical implementation allows computing hundreds of thousands of fractal surfaces within hours. The bolometric albedo A_{dh}, the directional emissivity, and the remaining reflectance component are inferred from Moon Mineralogy Mapper data [1] with the Hapke model [4].

Model accuracy: We validated the model with two datasets: First, it agrees well with disk-resolved lunar telescopic measurements under moderate phase angles (25° and 30°) acquired with the mid-infrared sensor (around 3.77 µm) of the Chinese Gaofen-4 Earth-observation satellite [5]. The surface roughness successfully reproduces the enhanced thermal emission near the lunar rim, and the digital elevation model and disk-resolved albedo maps capture local features. However, minor deviations occur in titanium-rich regions and at bright ejecta blankets, presumably because the albedo estimates could not fully capture these effects. Overall, the root-mean-squared error between the modeled and the measured infrared spectra is about 3%, averaging over all sixteen profiles shown in [1]. Second, the model was compared to nadir and more extreme off-nadir measurements of the Diviner lunar radiometer onboard the Lunar Reconnaissance Orbiter [6]. The model agrees well with measurements from the narrow-band channel four (around 8.25 µm) and the broadband channel seven (between 25-41 µm) of the Diviner lunar radiometer. The model has further been compared to lunar flyby measurements of the MErcury Radiometer and Thermal Infrared Spectrometer (MERTIS) onboard the BepiColombo spacecraft [7]. The calibration baffle of MERTIS pointed toward the Moon, and six pixels scanned the lunar surface. The measurements and the model show good agreement in four broad wavelength bins between 7-14 µm, but the observation conditions introduced considerable uncertainty, prohibiting more detailed evaluation.

Future activities: The model accurately reproduces the spectral radiance for the given datasets. However, Gaofen-4 measurements around 3.77 µm predict roughness values of around 20°, and Diviner off-nadir measurements around 8.25 µm predict roughness values of around 30°. Earlier studies [6] report similar findings, which call for exploring anisotropic emissivity modeling and its interplay with directional-hemispherical albedo and roughness for more extreme geometric configurations. Datasets that cover more phase angles and wavelengths will help investigate this aspect and improve the model.

References

[1] Wohlfarth, K., Wöhler, C., Hiesinger, H., Helbert, J. (2023) An advanced thermal roughness model for airless planetary bodies - Implications for global variations of lunar hydration and mineralogical mapping of Mercury with the MERTIS spectrometer. Astronomy & Astrophysics, 674, A69. 10.1051/0004-6361/202245343

[2] Helfenstein, P. and Shepard, M. K. (1999) Submillimeter-Scale Topography of the Lunar Regolith. Icarus 141 (1), 107- 31. 10.1006/icar.1999.6160

[3] Rozitis, B. and Green, S. F. (2011) Directional characteristics of thermal–infrared beaming from atmosphereless planetary surfaces – a new thermophysical model. MNRAS 415(3), 2042-2062. 10.1111/j.1365-2966.2011.18718.x

[4] Hapke, B. (2012) Theory of Reflectance and Emittance Spectroscopy. Cambridge Univ. Press

[5] Wu, Y., Jin, Q., Li, C., Xu, T., Qi, W., Tan, W., Li, X., Shi, Z., He, H., Dai, S., Li, G., Liu, F., Wang, J., Wang X., Lu, Y., Cai, W., Wang, Qi., Meng, L., Guo, D. (2021) Unveiling the secrets of the mid-infrared (3-5 µm) Moon. Geophysical Research Letters, 48, e2020GL088393. 10.1029/2020GL088393

[6] Bandfield, J. L., Hayne, P. O., Williams, J.-P., Greenhagen, B. T., Paige, D. A. (2015) Lunar surface roughness derived from LRO Diviner Radiometer Observations. Icarus 248, 357-372. 10.1016/j.icarus.2014.11.009

[7] Hiesinger, H., Helbert, J., Bauch, K., D'Amore, M., Maturilli, M., Morlok, A., Reitze, M., Stojic, A. N., Varatharajan, I., Weber, I., Wohlfarth, K., Wöhler, C. (2021) The Mercury Radiometer and Thermal Infrared Spectrometer (MERTIS) at the Moon - First Results and Status Report. LPSC LII, abstract # 149.

doi: 10.25923/6c4m-y998

Summary of recent AIRS/IASI/CrIS SNO comparison Paper

By David Tobin and Michelle Loveless (University of Wisconsin-Madison)

"Comparison of the AIRS, IASI, and CrIS Infrared Sounders using Simultaneous Nadir Overpasses: Novel methods applied to data from 1 October 2019 to 1 October 2020" was recently published by Loveless et al. This paper presents a refinement of the methodology used to intercompare observed spectra from the GSICS hyperspectral IR reference sensors. The refinements include the use of spatial sampling uncertainties to weight the value of each SNO in an ensemble, and a SNO time difference symmetrization process. Where possible, scene dependent radiometric measurement uncertainties are included and propagated through the statistics. Results for Aqua AIRS, Metop-A, B, and C IASI, and S-NPP and NOAA-20 CrIS, for northern and southern hemisphere SNOs over the one-year period are presented in a number of ways. Differences between the various measurements are found to be generally less than 0.1 or 0.2 K.

To obtain a useful number of SNOs between CrIS and IASI within a relatively short time period, the SNO time difference can be as large as 40 minutes. Consistent with some other findings, the study demonstrates that for some parts of the spectrum (layers of the atmosphere) there is an important correlation of the SNO bias with SNO time difference (i.e. Figure 1 of the paper for the 720 cm^{-1} region). One hypothesis for this effect is the diurnal warming of the stratosphere. Therefore, a SNO ensemble with an asymmetric distribution of time differences will lead to erroneously derived biases. To account for this effect the time symmetrization process described in Section 3.4 of the paper is introduced.

As one example result, Figures 9 and 10 of the paper show differences as a function of scene temperature. The shortwave window region (2500 to 2520 cm^{-1}) comparisons at the CrIS Internal Calibration Target (ICT) (aka blackbody) temperature of approximately 280K are particularly useful for assessing the accuracy of the CrIS ICT predicted radiance, which is a key component of the CrIS calibration. This is because the CrIS calibration in this spectral region is linear and has negligible influence from polarization correction uncertainty for scene temperatures near the ICT (and scan mirror) temperature. The SNO comparisons for these conditions show agreement between all sensors within the associated comparison (sampling) uncertainties and with differences less than the CrIS Radiometric Uncertainty.

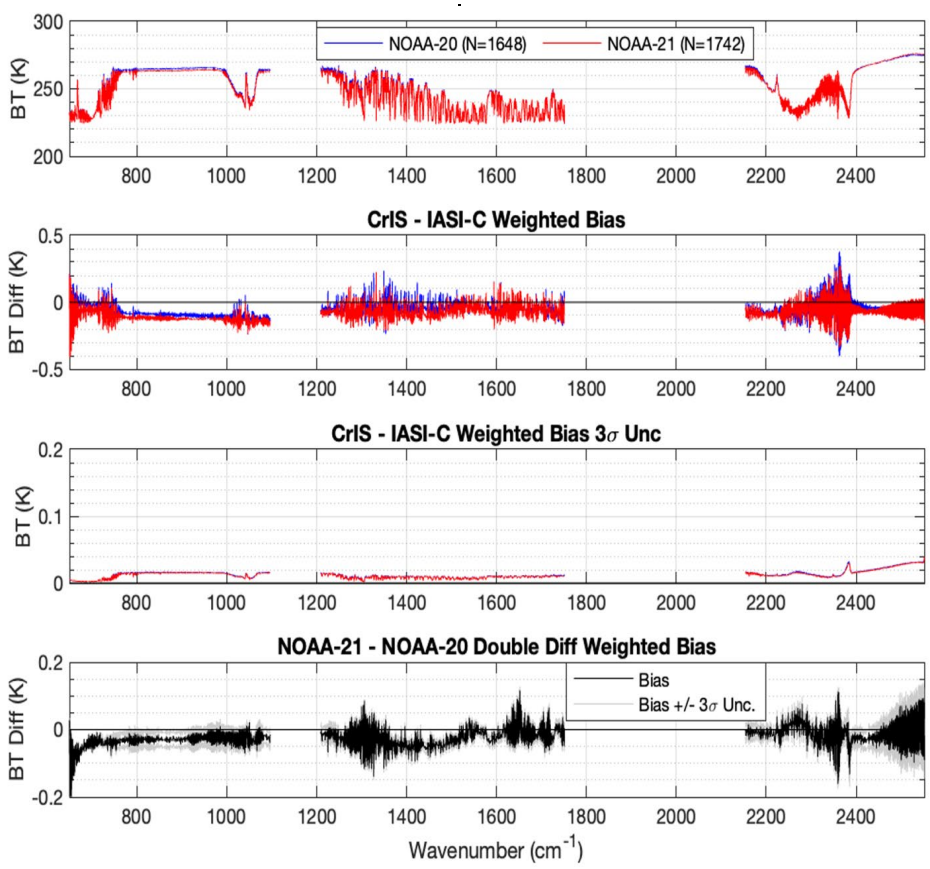

Figure 1. Comparisons of NOAA-20 CrIS, NOAA-21 CrIS, and Metop-C IASI, using Northern hemisphere SNOs collected from 23 March to 31 August 2023. Top panel: Mean spectra. Second panel: Weight mean differences between NOAA-21 CrIS and IASI (red) and NOAA-20 CrIS and IASI (blue). Third panel: Spatial sampling uncertainties for NOAA-21 (red) and NOAA-20 (blue). Bottom panel: Double differences between NOAA-21 CrIS and NOAA-20 CrIS.

The same comparison methodology described in the paper was recently used in the evaluation of NOAA-21 CrIS as part of the post-launch evaluation effort. An example result in Figure 1 shows the comparisons of NOAA-20 CrIS and NOAA-21 CrIS with Metop-C IASI, and the double difference of NOAA-21 CrIS with NOAA-20 CrIS. Mean differences between IASI and the two CrISes are less than approximately 0.2K, and the differences between the

doi: 10.25923/6c4m-y998

two CrISes are less than approximately 0.1K. These differences are less than the reported Radiometric Uncertainty of CrIS. The 3-sigma spatial sampling uncertainty in these determinations, which is the largest contributor to the total inter-comparison uncertainty, is shown in the third panel and less than approximately 0.02K. These results, and those presented in the journal article, support the use of data from these sensors as GSICS reference data that can be used for intercomparisons with data from other hyperspectral and broadband sensors.

Reference:

Loveless, M., Knuteson, R., Revercomb, H., Borg, L., DeSlover, D., Martin, G., Taylor, J., Iturbide-Sanchez, F., Tobin, D., 2023, Comparison of the AIRS, IASI, and CrIS Infrared Sounders using Simultaneous Nadir Overpasses: Novel methods applied to data from 1 October 2019 to 1 October 2020. *Earth and Space Science*, 10, 10.1029/2023EA002878.

NEWS IN THIS QUARTER

Highlights of 2023 EUMETSAT Meteorological Satellite Conference

By Tim Hewison (EUMETSAT) and Manik Bali (NOAA/CICS)

This year the EUMETSAT Meteorological Satellite conference took place at Malmö, Sweden from 11-15 September 2023. It was hosted by the Swedish Meteorological and Hydrological Institute (SMHI), the national provider for weather, water and climate services in Sweden.

The theme this year was "Evolutionary challenge for EO satellites from technology to exploitation". The conference started with a plenary session on applications of existing and future Earth Observation missions of EUMETSAT, NOAA, Korea, China and others and the conference spanned vital topics which included

- Present and future horizons for satellite programmes
- High impact weather forecasting – including a special session on MTG (Meteosat Third Generation)
- Applications in energy meteorology in support of energy security
- Advancing in the digital transformation of our community, from the European weather cloud to AI/ML and big data
- Assessing climate variability and change using satellite observations
- Atmospheric composition including greenhouse gasses
- Drought and vegetation monitoring for food security and hydrological applications
- New methods to exploit and visualize EO data
- Ocean interface
- New space and the opportunities of small satellites

From a GSICS perspective, highlights included a session on Calibration and Validation and several posters and talks presented on Satellite calibration. Some of these are:

- Michela Sunda (EUMETSAT) reported on EPS-SG Commissioning Phase and the Calibration/Validation Activities Preparation. She mentioned that IASI-NG (potential GSICS Reference) would be commissioned within nine months of launch of the Metop-SG-A platform. Comparison of instruments onboard the EPS-SG platforms with other satellite data via international partner agencies, GSICS, CEOS, WG Climate etc. is also a key CAL/VAL activity planned for the mission.

doi: 10.25923/6c4m-y998

- On EUMETSAT's new Meteosat Third Generation:
  - Tim Hewison presented comparisons of the Flexible Combined Imager (FCI), the MTG-I1/FCI with MSG/SEVIRI and IASI by using the GSICS (GEO-GEO and GEO-LEO) inter-comparison algorithms. The FCI is in commissioning phase and was not yet radiometrically corrected. This comparison helped understand processing and diurnal artifacts in FCI and would directly aid in radiometrically tuning the FCI to make it operational.
  - Sven-Erik Enno described the Monitoring of Meteosat Third Generation Lightning Imager (LI) Level-1b and Level-2 product performance during routine operations and commissioning.
- Lei Yang (CMA) presented navigation and calibration performance assessment for Geostationary High-speed Imager onboard FY4B. Lei reports that navigation accuracy of the GHI has reached 2km(3σ) and the GHI IR images mean brightness temperature (Tb) bias with respect to Metop-B/IASI of less than 0.7K. A series of presentations addressed various instruments on the Joint Polar Satellite System (JPSS) onboard NOAA-21.
  - Lihang Zhou (NOAA) gave an overview of instruments. ATMS, VIIRS, OMPS and CrIS on board NOAA-21 are now producing operational L1 data. These instruments may go on to become GSICS reference instruments.
  - Wenhui Wang (University of Maryland) gave an overview of post launch performance of VIIRS.
  - Xiaoxiong (Jack) Xiong (NASA) reviewed the performance of the VIIRS on board NOAA-21. He compared the on-board calibration with Solar and Lunar views by the VIIRS instrument.
- Flavio Iturbide Sanchez (NOAA) revealed the performance of CrIS (GSICS Reference instrument) instrument onboard the NOAA-21 and its impact on the NWP systems. He indicated that NOAA-21/CrIS would continue to provide high quality measurements and would reach validation state soon.
- Martin McHugh (NOAA) provided an overview of the Space Weather and commercial satellites data pilot program
- Antonia Gambacorta (NASA) introduced the Hyperspectral Microwave Photonic Instrument (HyMPI), which includes technology that could be of interest to GSICS microwave sub-group for future reference instruments, to improve spectroscopy and RFI rejection.
- Several presentations on constellations of Earth Observation satellites built by New Space companies were especially interesting for the GSICS members and have opened up a window of opportunity for GSICS - Newspace collaboration.

The presentations will be available on the EUMETSAT conference website: https://www.eumetsat.int/eumetsat-meteorological-satellite-conference-2023

Announcements

Workshop on Pre-flight Calibration and Characterization of Optical Satellite Instruments for Earth Observation to be held 19-22 November 2024 at ESTEC, Noordwijk, Netherlands

By Nigel Fox (NPL) and Xiaoxiong (Jack) Xiong (NASA)

The workshop seeks to bring together, experts from industrial and academic developers of instruments, those specifying, designing and performing calibration and characterisation as well as scientists, engineers, New Space actors, agencies and funding organisations interested in: what is and/or might be possible for a next generation instrument or future application. The workshop will be organised to encourage discussion and debate on what is 'fit for purpose' for particular types of application.

UV to SWIR and TIR:

- Future Calibration / Characterisation Requirements
- Principles of Calibration / Characterisation / Traceability / Uncertainty and its Documentation / Reporting
- Spectral Response Function / Bandwidth / Wavelength / Smile (Discrete bands & Spectrometers)

- Stray Light (Out-of-Field, Out-of-Band), Point Spread Function, Ghosts, Scattered
- Radiometric Gain / Non-Linearity / Polarisation Sensitivity

Workshop Website: https://atpi.eventsair.com/pre-flight-calibration-workshop/

GSICS-Related Publications

Castillo, A. M., Shprits, Y. Y., Aseev, N. A., Smirnov, A., Drozdov, A., Cervantes, S., et al. (2024). Can we intercalibrate satellite measurements by means of data assimilation? An attempt on LEO satellites. Space Weather, 22, e2023SW003624. https://doi.org/10.1029/2023SW003624

H. Wang *et al*., "Preflight Calibration of Short-Wave Infrared Polarization and Multiangle Imager Onboard Fengyun-3 Satellite," in *IEEE Transactions on Geoscience and Remote Sensing*, vol. 62, pp. 1-12, 2024, Art no. 5610612, doi: https://doi.org/10.1109/TGRS.2024.3366702

Jiang, X.; Zhang, X.; Liu, M.; Tian, J. Joint Panchromatic and Multispectral Geometric Calibration Method for the DS-1 Satellite. *Remote Sens.* **2024**, *16*, 433. https://doi.org/10.3390/rs16020433

L. Yan, Y. Hu, C. Dou and X. -M. Li, "Radiometric Calibration of SDGSAT-1 Nighttime Light Payload," in *IEEE Transactions on Geoscience and Remote Sensing*, vol. 62, pp. 1-15, 2024, Art no. 1000715, doi: https://doi.org/10.1109/TGRS.2024.3370572

Paszkuta, M., M. Markowski, and A. Krężel, 2024: Empirical Verification of Satellite Data on Solar Radiation and Cloud Cover over the Baltic Sea. *J. Atmos. Oceanic Technol.*, **41**, 161–178, https://doi.org/10.1175/JTECH-D-23-0061.1.

Thankappan, M.; Christopherson, J.; Cantrell, S.; Ryan, R.; Pagnutti, M.; Bright, C.; Naughton, D.; Ruslander, K.; Wang, L.; Hudson, D.; Shaw, J.; Ramaseri Chandra, S.N.; Anderson, C. Concept of a Satellite Cross-Calibration Radiometer for in-orbit Calibration of Commercial Optical Satellites. Preprints 2024, 2024021516. https://doi.org/10.20944/preprints202402.1516.v1

W. Wu *et al*., "The Angular Correction Algorithm for the Intercalibration of Satellite Instruments Using CLARREO Pathfinder as a Reference," in *IEEE Transactions on Geoscience and Remote Sensing*, vol. 62, pp. 1-11, 2024, Art no. 5507211, doi: https://doi.org/10.1109/TGRS.2024.3359972

Xu, Z.; Sun, R.; Wu, S.; Shao, J.; Chen, J. Inter-Calibration of Passive Microwave Satellite Brightness Temperature Observations between FY-3D/MWRI and GCOM-W1/AMSR2. *Remote Sens.* **2024**, *16*, 424. https://doi.org/10.3390/rs16020424

Submitting Articles to the GSICS Quarterly Newsletter:

The GSICS Quarterly Press Crew is looking for short articles (800 to 900 words with one or two key, simple illustrations), especially related to calibration / validation capabilities and how they have been used to positively impact weather and climate products. Unsolicited articles may be submitted for consideration anytime, and if accepted, will be published in the next available newsletter issue after approval / editing. Please send articles to manik.bali@noaa.gov.

With Help from our friends:

The GSICS Quarterly Editor would like to thank Tim Hewison (EUMETSAT) and Lawrence Flynn (NOAA) for reviewing articles in this issue. Thanks are due to Jan Thomas (NOAA) for helping with 508 compliance.

doi: 10.25923/6c4m-y998

Published By

GSICS Coordination Center
NOAA/NESDIS/STAR NOAA
Center for Weather and Climate Prediction,
5830 University Research Court
College Park, MD 20740, USA

CISESS
5825 University Research Court, Suite 4001,
University of Maryland, College Park, MD 20740-3823